Medical Engineering and Physics 97 (2021) 1–9

Contents lists available at ScienceDirect

Medical Engineering and Physics

journal homepage: www.elsevier.com/locate/medengphy

# Tidal spirometric curves obtained from a nasal cannula

Rutger H.J. Hebbink *, Rob Hagmeijer

*Engineering Fluid Dynamics, University of Twente, PO Box 217, AE Enschede 7500, The Netherlands*

ARTICLE INFO

*Keywords:*
Flow-volume curves
Obstructive lung diseases
Nasal cannula
Tidal spirometry

ABSTRACT

Spirometry is a gold standard to assess lung function, and to identify respiratory impairments seen in obstructive lung diseases. The method is used for periodic monitoring, but it only provides snapshot information, and it requires forceful exhalation which is associated with limited reliability and repeatability. Several studies indicate that tidal flow-volume curves measured by pneumotachography or plethysmography can also be used to assess lung function. These methods avoid the forced manoeuvre, but are complex to set up or sensitive to movement. In the present work we address the long-standing problem of the unavailability of an easy-to-use and accurate method for monitoring tidal breathing frequently or even continuously. We show that pressure recordings from a nasal cannula can be accurately converted into scaled flow-volume curves by means of an algorithm that continuously calibrates itself. The method has been validated by feeding realistic healthy and unhealthy breathing patterns to anatomically correct 3D-printed upper airways of an infant and an adult, and by comparing the imposed flow-volume curves to the pressure-derived flow-volume curves. The observed very high level of accuracy opens the route towards remotely monitoring patients with chronic lung diseases.

## 1. Introduction

Spirometry is a gold standard to test lung function, and thereby to support the diagnosis of different obstructive lung diseases and to periodically monitor disease progression [1–3]. During a spirometry test, flow-volume curves are obtained by letting the patient maximally inhale and forcefully exhale through a mouth piece [3]. The shape of the flow-volume curves can be used as an indication of several obstructive lung diseases such as asthma and Chronic Obstructive Pulmonary Disease (COPD), and their severity [1,3]. Unfortunately, the required forced expiration manoeuvre is associated with limited reliability and repeatability [3,4]. Especially for patients with severe pulmonary diseases and for elderly people, the required effort for the forced expiration manoeuvre is problematic [5,6]. Furthermore, spirometry tests on infants may be difficult due to a lack of patient cooperation [5,7].

Though not a gold standard, upper airway obstruction can also be revealed by *tidal* spirometry. Evidence for the influence of obstructive lung diseases on tidal breathing profiles has been presented in several studies on both infants [7–9] and adults [10–13]. Various methods are used to obtain tidal spirometric curves. The most common one is pneumotachography (PNT) [14], in which patients are connected to a face mask or to a combination of a mouthpiece and a nose clip while the time-dependent flow rate is measured by a pneumotachograph. A disadvantage of this technique is that the breathing profile is altered because of the face mask or mouth piece [14–16]. Another disadvantage is encountered for neonates, where the dead space of the apparatus may exceed the infant's own dead space, limiting the time of measurement [9].

Tidal curves can also be obtained using plethysmographic methods based on the movement of the chest and abdominal wall. Respiratory inductance plethysmography (RIP) uses an elastic band to measure this movement, but the calibration required for obtaining flow and volume signals is problematic [17,18]. In opto-electronic plethysmography (OEP) the wall movement is measured from 52 to 89 reflective markers placed on the skin [13,18,19], requiring at least four cameras and two calibration procedures to determine the 3D-coordinates of each marker [18]. Structured light plethysmography (SLP) is a non-contact method, where the position of points in a structured grid, which is projected onto the patient, are used to record chest wall movement [20]. Although the technique is non-invasive and quick to set up, it is sensitive to movement, and even lightly moving arms or legs or rotating the head may affect the measurements [20].

Another way to determine lung function during tidal breathing is by using oscillometry, as used in the forced oscillation technique (FOT) and impulse oscillometry (IOS). Single (FOT) or mulitple (IOS) frequency sound waves (pressure pulses) are pushed into the airways during tidal

* Corresponding author.
*E-mail addresses:* r.h.j.hebbink@utwente.nl (R.H.J. Hebbink), r.hagmeijer@utwente.nl (R. Hagmeijer).

https://doi.org/10.1016/j.medengphy.2021.09.004
Received 4 August 2021; Received in revised form 13 September 2021; Accepted 14 September 2021
Available online 16 September 2021

breathing, and the respiratory resistance and reactance are measured [21,22]. Although the variability is higher than in (forced) spirometry tests, the sensitivity to detect airway obstruction is better [21–23]. In a way these methods can be seen as an extension of pneumotachography: patients are still leak-free connected to the combination of a mouthpiece and a nose clip while measuring the flow rate, while additionally pressure pulses are superimposed to the breathing and pressure is measured in the device.

To circumvent the problems encountered in leak-free flow-rate measurements or plethysmographic methods, one can alternatively measure pressure, by for example using a nasal cannula encountered in nasal high-flow therapy or oxygen therapy. This idea was applied in studies to record respiratory events during sleep [24–27], and Hosselet et al. used it to determine inspiratory flow limitation [28]. Although the inspiratory flow rate could not be quantified it was assumed to be linearly dependent on the nasal cannula pressure, and flow limitation was detected by plotting the nasal cannula pressure versus the driving (supraglottic or esophageal) pressure. However, this method can be seen as invasive and patient-unfriendly because of the need for an esophageal or supraglottic catheter. Kohler et al. [29,30] quantified nasal airflow using a modified nasal cannula (with the two sides disconnected) and two pressure transducers, but their method requires a calibration of the pressure to the flow by using a nasal mask with a flow meter attached.

In general, any calibration prior to the application of a method requires time to set up and may cause errors over the course of the measurements due to changing circumstances. In this work, a novel, *continuously auto-calibrating* algorithm is presented to reconstruct *scaled* tidal spirometric flow-volume curves from nasal pressure measurements. The underlying observation is that from a clinical point of view it is primarily the *shape* of the spirometric curve that is of interest. This view is supported by several studies demonstrating the significance of the shape of tidal flow-volume curves [6,8,9,31] in the identification of chronic lung diseases, and demonstrating the use of scaled tidal breathing parameters [7,32] in the identification of expiratory airway obstruction.

The main objective of this work is to present the derivation of the reconstruction method, and to demonstrate its feasibility and validity. To validate the proposed reconstruction method the actual flow-volume curves have to be known with sufficient accuracy. Therefore, instead of relying on *in-vivo* measurements, experiments with anatomically correct 3D-printed upper airway geometries and simulated breathing were conducted. The clinical applicability of the method will be addressed in future work. The paper is organised as follows. First the method to reconstruct scaled flow-volume curves from pressure recordings is presented. Secondly, the experimental method is described, based on 3D-printed upper airways of an infant and an adult. Thirdly, a comparison of the actual and reconstructed flow-volume curves is presented for healthy and obstructed respiration profiles. Finally, the results are discussed and a perspective on future research is given.

## 2. Reconstruction method

Upon inserting a nasal cannula into the nose, there is a difference between the cannula pressure and the ambient pressure caused by the aerodynamic resistance of the flow annulus enclosed by the nostrils and the prongs (tubes of the cannula), see the schematic impression in Fig. 1. During the periodic transition between inspiration and expiration, the flow direction, flow topology, and nostril geometry change, which results in a change of the aerodynamic resistance. The challenge one faces to accurately quantify the flow rate from the pressure difference is to accurately quantify the aerodynamic resistance, which of course is difficult in clinical practice. The key idea of the presented reconstruction method is to reconstruct *scaled* tidal spirometric flow-volume curves from the pressure recordings which do *not* require the values of these resistances.

The inserted cannula is schematically depicted in Fig. 1, indicating

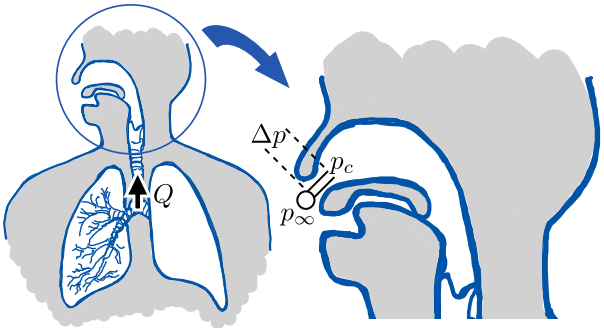


**Fig. 1.** Schematic representation of a nostril with cannula, with pressure difference $\Delta p = p_c - p_\infty$, and the trachea with flow rate $Q$ (illustrated direction defined positive).

the flow rate $Q$ at the trachea, defined positive when exhaling, and the difference $\Delta p$ between the pressure at the end of the cannula, $p_c$, and the atmospheric pressure, $p_\infty$. From a fluid mechanics point of view, $Q$ and $\Delta p$ are interdependent, and to account for a nonlinear relationship a power-law is assumed:

$$Q(t) = a|\Delta p(t)|^b, \quad \text{sign}(a) = \text{sign}(\Delta p), \tag{1}$$

that differs between inspiration and expiration by letting the constants $a$ and $b$ both depend on the sign of $\Delta p$,

$$a = \begin{cases} a_{in}, & \Delta p < 0, \\ a_{ex}, & \Delta p \geq 0, \end{cases} \quad b = \begin{cases} b_{in}, & \Delta p < 0, \\ b_{ex}, & \Delta p \geq 0, \end{cases} \tag{2}$$

with $a_{in} < 0$, $a_{ex} > 0$, $b_{in} > 0$, and $b_{ex} > 0$. Eq. (2) reflects that the aerodynamic resistance not only depends on the geometry of the flow tube, but also on the direction of the flow and on the flow condition. The limits of $b$ are theoretically known: $b = 1$ indicates fully laminar flow and $b = 1/2$ indicates fully turbulent flow. It is noted that this model allows for elastic walls that have a different shape during inhalation and exhalation and for density differences between inhaled and exhaled air, as the proportionality constants $a$ will account for all of these effects. However, the values of these constants are variable and unknown in a clinical setting.

The net exhaled volume $V(t)$ is obtained by integration of the flow rate $Q(t)$ over time $t$:

$$V(t) = \int_0^t Q(\tau) d\tau. \tag{3}$$

To derive the scaled flow-volume curve, $V(t)$ is split into the exhaled volume $V_{ex}(t)$ and the inhaled volume $V_{in}(t)$ as

$$V(t) = V_{in}(t) + V_{ex}(t), \tag{4}$$

with the two parts defined as

$$\begin{aligned} V_{ex}(t) &\equiv \int_0^t \max(0, Q(\tau)) d\tau \geq 0, \\ V_{in}(t) &\equiv \int_0^t \min(0, Q(\tau)) d\tau \leq 0. \end{aligned} \tag{5}$$

Using the power laws given by Eqs. (1) and (2), these expressions can be written as

$$V_{in}(t) = -a_{in} I_{in}(t), \quad V_{ex}(t) = a_{ex} I_{ex}(t), \tag{6}$$

with

$$\begin{aligned} I_{in}(t) &\equiv \int_0^t \min(0, \text{sign}(\Delta p)) |\Delta p|^b d\tau \leq 0, \\ I_{ex}(t) &\equiv \int_0^t \max(0, \text{sign}(\Delta p)) |\Delta p|^b d\tau \geq 0. \end{aligned} \tag{7}$$

Let $T$ be the time needed to complete $K$ breathing cycles. To eliminate the difficulty of the case-dependent and unknown proportionality constants $a_{in}$ and $a_{ex}$, first the net exhaled volume is scaled as

$$\widetilde{V}(t) \equiv \frac{K\,V(t)}{V_{ex}(T)}. \tag{8}$$

Note that the scaling factor $V_{ex}(T)/K$ represents the average tidal volume over the $K$ cycles. Upon inserting Eqs. (4), (6) and (7), this scaling leads to

$$\widetilde{V}(t) = K\left(\frac{I_{ex}(t)}{I_{ex}(T)} - \frac{a_{in}}{a_{ex}}\frac{I_{in}(t)}{I_{ex}(T)}\right). \tag{9}$$

Hence, the scaled volume is not determined by the individual values of $a_{in}$ and $a_{ex}$, but only by their ratio.

To also eliminate this ratio, $K$ is chosen relatively large compared to 1, typically $K \approx 10$. If $K$ is large, $T$ is large, and both $-V_{in}(T)$ and $V_{ex}(T)$ become large. Their absolute difference changes with time, but is bounded by the vital lung capacity and typically proportional to the tidal volume. Their relative difference however tends to zero, and the ratio $-V_{in}(T)/V_{ex}(T)$ tends to one. As a result,

$$\lim_{K\to\infty}\frac{a_{in}}{a_{ex}} = \frac{I_{ex}(T)}{I_{in}(T)}. \tag{10}$$

Substitution of this limit into Eq. (9) leads to a convenient approximation of the scaled net exhaled volume, free of the case-dependent proportionality constants $a_{in}$ and $a_{ex}$:

$$\widetilde{V}(t) \approx K\left(\frac{I_{ex}(t)}{I_{ex}(T)} - \frac{I_{in}(t)}{I_{in}(T)}\right). \tag{11}$$

In a natural way, the corresponding scaled flow rate is defined as the non-dimensional time derivative of the scaled volume:

$$\widetilde{Q}(t) \equiv \frac{T}{2\pi K}\frac{d\widetilde{V}(t)}{dt}, \tag{12}$$

where the factor $2\pi K/T$ represents the average angular frequency of the respiration signal. Evaluation of the above expression leads to

$$\widetilde{Q}(t) = \begin{cases} |\Delta p|^{b_{in}} T \Big/ (2\pi I_{in}(T)), & \Delta p < 0, \\ |\Delta p|^{b_{ex}} T \Big/ (2\pi I_{ex}(T)), & \Delta p \geq 0. \end{cases} \tag{13}$$

The values of the remaining exponents $b_{in}$ and $b_{ex}$ and the sensitivity to these values will be determined experimentally.

## 3. Validation method

In-vitro experiments were performed to determine values for the constants $b_{in}$ and $b_{ex}$, the sensitivity to these values, and how well the shape of the imposed flow-volume curves is reconstructed from pressure measurements. Two things were measured: (a) the pressure at the end of the cannula, and (b) the position of the piston of a breathing simulator. The pressure is used to reconstruct the scaled flow and volume using the method described above, while the piston position is used to compute the actual flow and volume.

### 3.1. Experimental setup

A semi-schematic overview of the experimental setup is shown in Fig. 2. Anatomically accurate 3D-printed upper airway geometries with artificial breathing were used. Different breathing profiles were simulated by the breathing simulator while pressure was recorded via a nasal cannula. The pressure was used to reconstruct $\widetilde{Q}(t)$ and $\widetilde{V}(t)$ signals following Eqs. (13) and (11). These signals were compared to the actual signals, which were determined from the recorded volume change of the breathing simulator.

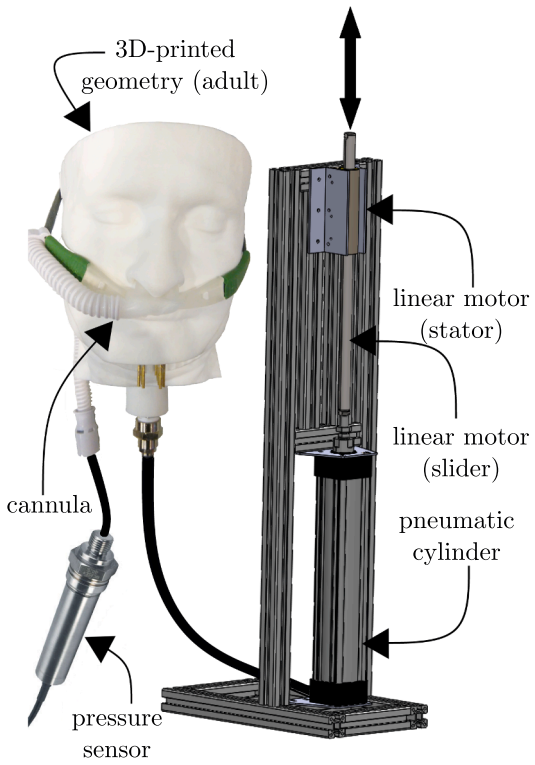


**Fig. 2.** Semi-schematic overview of the experimental setup. Components are not to scale.

Two different upper-airway geometries were used: one of a 9 month old Caucasian girl, known as the SAINT-model [33], and one of a male adult, obtained from [34] and modified (by removing details outside the airway and adding connections) with permission from the author. In both models, the oral airway was closed for air passage. The infant model was printed using Digital Light Processing (DLP) with EnvisionTEC RC31 material, whereas the adult model was printed using Selective Laser Sintering (SLS) with PA 12 nylon, and impregnated afterwards to prevent air leakage.

A breathing simulator was connected to the trachea, see Fig. 2. The breathing simulator consisted of a linear motor (stator: LinMot PS01-37Sx120F-HP-N, slider: LinMot PL01-20x500/440-HP) rigidly connected to a pneumatic cylinder (Parker P1D-S032MS-0320 for the infant and Parker P1D-S063MS-0320 for the adult). The motion of the motor was prescribed and, to verify the produced breathing flow rate, the position of the pneumatic cylinders was monitored using a magnetic sensor (Parker P8SAGACHH) with a sampling frequency of 500 Hz. Position data was filtered using a moving mean filter with 25 points. The displaced volume was determined by multiplying the axial displacement by the cross-sectional area, and the flow rate was obtained by differentiating the volume with respect to time.

An aerodynamic resistance was introduced by placing a nasal cannula in the nose of the 3D-printed models. For the infant model, three different cannula sizes were used: small (OPT312, labeled premature), medium (OPT314, labeled neonatal) and large (OPT316, labeled infant) (Optiflow Junior nasal cannula, Fisher & Paykel Healthcare Ltd., New Zealand). Also for the adult, three different cannula sizes were used: small (OPT942), medium (OPT944), and large (OPT946) (Optiflow+ nasal cannula, Fisher & Paykel Healthcare Ltd., New Zealand). Images of these cannulae placed in the noses of the models are shown in Fig. 3. It is noted that the large cannula in the infant model almost fully occludes the nose. The corresponding high aerodynamic resistance and increased work of breathing are of course unacceptable in clinical practice, but the experimental data have still be included in this work for reasons of

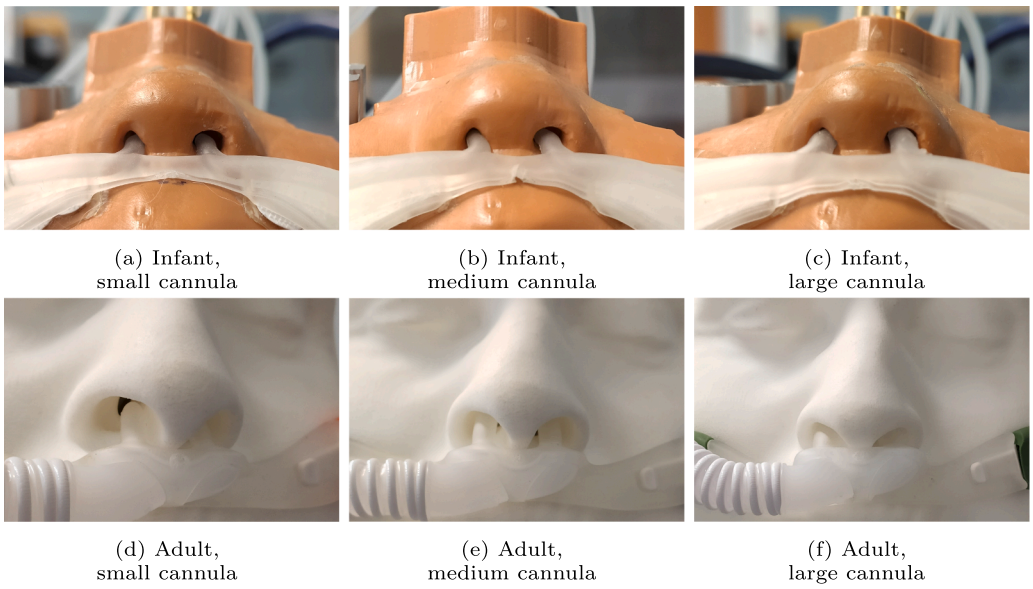

(a) Infant, small cannula (b) Infant, medium cannula (c) Infant, large cannula

(d) Adult, small cannula (e) Adult, medium cannula (f) Adult, large cannula

**Fig. 3.** The two models with the three cannula sizes.

completeness.

The cannula was connected to a dead-end circuit, where a pressure transducer (Omega PXM409-070HCGUSBH, range of ± 7000 Pa) recorded the pressure (relative to atmosphere) at a sampling frequency of 160 Hz. The sensor was zeroed by subtracting the average pressure over 10 s without flow before each measurement. Data was filtered using a low-pass filter with a cut-off frequency of $10f_b$, where the breathing frequency $f_b$ was estimated based on the local minima in the pressure signal. After that, separate breathing cycles were obtained from the filtered pressure signal based on local minima, such that a cycle starts and ends at peak inhalation. This was preferred over starting at zero flow because it is easier to detect in noisy signals.

### 3.2. Breathing profiles

Different representative tidal breathing profiles were obtained from literature and prescribed to the breathing simulator. For the infant model, non-obstructed (NO), moderately obstructed (MO) and severely obstructed (SO) profiles, all obtained from ref. [7], were simulated. For the adult model, a healthy profile [35] and a COPD-profile [6] were simulated. In both cases, the profiles were determined by applying image analysis to the figures from literature. The image-based profiles were smoothed and closed using a Fourier series with 20 frequencies. After that, the profiles were scaled to match chosen tidal volumes and cycle lengths: 85 mL and 1.76 s for the infant and 450 mL and 4 s for the adult. These numbers were close to the used healthy profiles. The resulting profiles are presented in Fig. 4 for the infant and in Fig. 5 for the adult.

In order to simulate more natural breathing, a sequence of 20 different breathing cycles (inhalation followed by exhalation) was constructed, where the net volume was allowed to be non-zero in each separate cycle, but constructed to be zero after the 20 cycles. This was done to allow for the repetitive movement of the breathing profile with the simulator. For each cycle, a pseudo-random difference for the net volume, $V_{in} + V_{ex}$, of maximally ±10% of the specified tidal volume was imposed. Inspiratory volume was increased in the case of negative net volume, whereas expiratory volume was increased in the case of positive net volume. In addition, the cycle times were allowed to vary randomly with ±0.25 s for the infant and ±0.5 s for the adult. Since the volume is scaled by a constant, and the flow rate is scaled by another constant, the shape of the profile doesn't change except for stretching in one direction. Following the procedure described above, the result based on the healthy profile for the adult, depicted in Fig. 5, leads to the profile shown in Fig. 6. All other profiles in Figs. 4 and 5 were treated similarly and the resulting sequences are labelled 'varying' in the remainder of this work.

Furthermore, a random test profile was simulated for the infant model with small cannula to demonstrate the robustness of the algorithm. This profile was not meant to be a representative respiration, but merely served as a challenging test for the reconstruction method. The test profile was constructed as a random Fourier series of 60 seconds with 60 frequencies. A total of 120 random numbers between -1 and 1 were generated for the Fourier coefficients, and these coefficients were linearly scaled such that the series spanned the maximum available stroke length of 255 mm.

### 3.3. Comparison of flow-volume curves

In order to compare two scaled flow-volume curves, an appropriate error needs to be defined which is insensitive for a time delay between the flow rate signals. If the air in the cylinder of the breathing simulator and within the upper airway geometry is fully incompressible, then the flow rate would be the same everywhere at any time instant, but in case of severe compressibility the flow rate at the nose of the model is different from the flow rate to or from the breathing simulator. However, mild compressibility effects are mainly observed as a small time delay between the measured volume change of the breathing simulator and the reconstructed flow rate [36,37]. It is observed that a time-shift $\tau_o$ of a flow rate signal leads to a volume-shift of the corresponding flow-volume curve:

$$\int_0^t Q(\tau+\tau_0)d\tau = V(t+\tau_0) - V(\tau_0). \tag{14}$$

Consequently, two flow rate signals $Q(t)$ and $Q(t+\tau_0)$ will lead to two flow-volume curves $(Q(t), V(t))$ and $(Q(t+\tau_o), V(t+\tau_o) - V(\tau_0))$ which have identical shapes but differ by a volume shift $-V(\tau_0)$. To compensate for this shift, the scaled volumes are translated as:

$$\widetilde{V}^*(t) \equiv \widetilde{V}(t) - \frac{1}{2}\left(\max\left(\widetilde{V}\right) + \min\left(\widetilde{V}\right)\right). \tag{15}$$

The error $\epsilon$ between two flow-volume curves $(Q_1(t), V_1(t))$ and $(Q_2(t), V_2(t))$, with time lapses $T_1$ and $T_2$ is now conveniently defined as

$$\epsilon \equiv \sqrt{\int_o^1 \left(\Delta\widetilde{V}_*(s)\right)^2 + \left(\Delta\widetilde{Q}_*(s)\right)^2 ds}, \tag{16}$$

where

$$\begin{aligned} \Delta\widetilde{V}_*(s) &\equiv \frac{\widetilde{V}_2^*(s\,T_2) - \widetilde{V}_1^*(s\,T_1)}{\max\left(\widetilde{V}_2^*\right) - \min\left(\widetilde{V}_2^*\right)}, \\ \Delta\widetilde{Q}_*(s) &\equiv \frac{\widetilde{Q}_2^*(s\,T_2) - \widetilde{Q}_1^*(s\,T_1)}{\max\left(\widetilde{Q}_2\right) - \min\left(\widetilde{Q}_2\right)}. \end{aligned} \tag{17}$$

## 4. Validation results

The accuracy of the reconstructed $\widetilde{Q}(t)$ and $\widetilde{V}(t)$ signals depends on the values of $b_{in}$ and $b_{ex}$. To determine which values of $b_{in}$ and $b_{ex}$ give the most accurate signals, the error $\epsilon$ was calculated for a range of values between 0.5 (fully turbulent flow) and 1 (fully laminar flow) for both models with one cannula and all reference breathing profiles (see Figs. 4 and 5). Although the optimal values for $b_{in}$ and $b_{ex}$ are different for every breathing profile, there is a relatively large region in the $(b_{in}, b_{ex})$ domain in which the error $\epsilon$ is quite insensitive to the values for $b$. The regions with the smallest errors are overlapping for the infant model with all breathing profiles and the adult model with healthy breathing, but is located at higher $b_{in}$ for the adult model with COPD breathing. In a clinical setting the optimal values for $b_{in}$ and $b_{ex}$ are unknown, and values need to be selected independent of the breathing profiles. Therefore, the average error over the different breathing profiles is calculated for both models, as shown in Fig. 7 for the infant and Fig. 8 for the adult. It can be seen that the average errors are relatively insensitive to the choice of $b_{in}$ and $b_{ex}$, and $b_{in} = 0.75$ and $b_{ex} = 0.55$ seem good choices for both the infant and the adult model. Note the clinical importance of this result: despite the significant differences between both geometries, fixed values for $b_{in}$ and $b_{ex}$ can be used to obtain reconstructed signals $\widetilde{Q}(t)$ and $\widetilde{V}(t)$ with low error $\epsilon$.

With the chosen values for $b_{in}$ and $b_{ex}$ it is possible to directly compare the reconstructed scaled flow-volume curves with the actual curves as measured from the position of the breathing simulator. In all cases, the assumption of Eq. (10) was applied over $K = 10$ breathing cycles. This number was considered representative for clinical use. For the infant with the small cannula, typically observed curves are shown in Fig. 9 for the different breathing profiles. It is seen that all reconstructed curves match almost perfectly with the actual curves that were determined from the position of the breathing simulator. Table 1 shows the values of $\epsilon$ for the small cannula for each of the 10 cycles used to determine the case-dependent ratio $a_{in}/a_{ex}$. Little variation is observed between the different cycles. To assess the effect of the cannula size, the

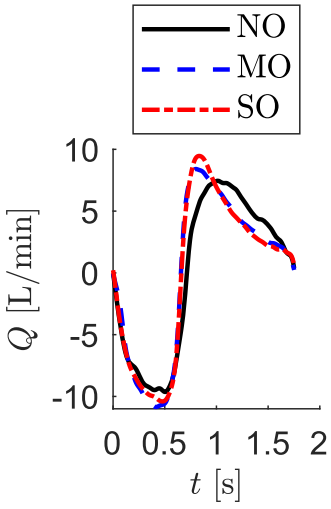


**Fig. 4.** Reference infant tidal breathing profiles [7] with no (NO), moderate (MO) and severe (SO) obstruction. Curves were scaled to a tidal volume of 85 mL and a length of 1.76 s.

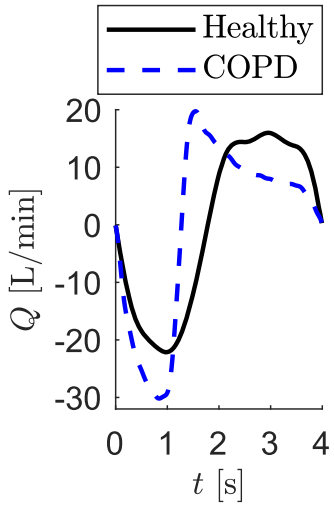


**Fig. 5.** Reference tidal breathing profiles of healthy adults [35] and COPD patients [6]. Both curves were scaled to a tidal volume of 450 mL and a length of 4 s.

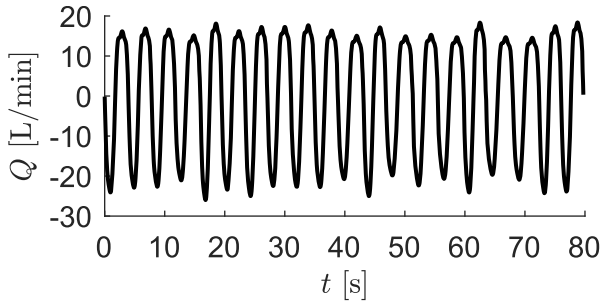


**Fig. 6.** Example of a varying breathing profile, derived from the healthy adult profile (solid line in Fig. 5). The cycles vary in flow rate, volume and cycle time.

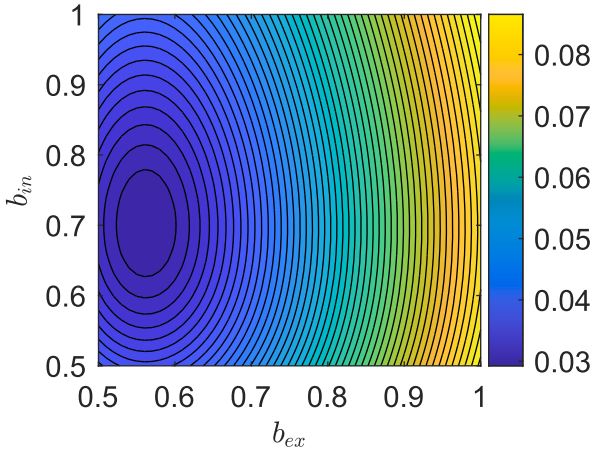


**Fig. 7.** The error $\epsilon$ for the infant model with small cannula, averaged (arithmetic) over the three breathing profiles of Fig. 4, for different values of $b_{in}$ and $b_{ex}$.

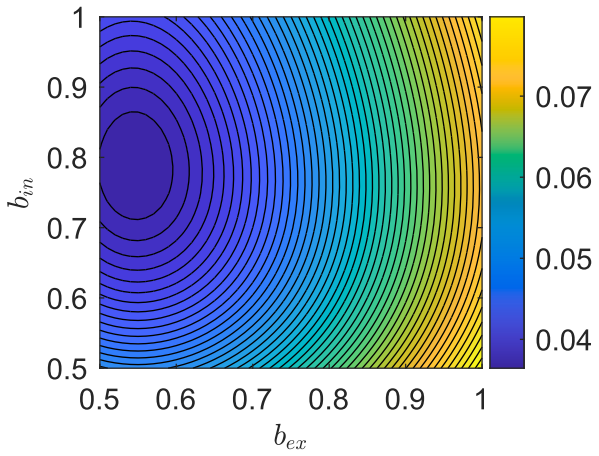


**Fig. 8.** The error $\epsilon$ for the adult model with large cannula, averaged (arithmetic) over the two breathing profiles of Fig. 5, for different values of $b_{in}$ and $b_{ex}$.

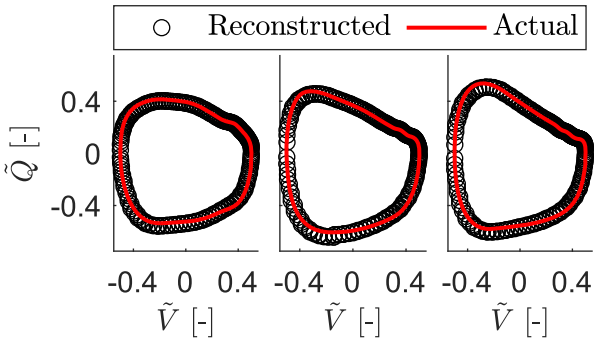


**Fig. 9.** Typical reconstructed and actual scaled flow-volume curves for non-obstructed (left, $\epsilon = 0.032$), moderately obstructed (middle, $\epsilon = 0.027$) and severely obstructed (right, $\epsilon = 0.024$) breathing for the infant model with small cannula.

**Table 1**
Values of $\epsilon$ for infant model with small cannula for ten cycles of the different breathing profiles (see Fig. 4).

| Cycle | NO | MO | SO | NO varying | MO varying | SO varying |
|---|---|---|---|---|---|---|
| 1 | 0.026 | 0.033 | 0.023 | 0.047 | 0.061 | 0.036 |
| 2 | 0.030 | 0.020 | 0.037 | 0.036 | 0.059 | 0.025 |
| 3 | 0.026 | 0.036 | 0.026 | 0.019 | 0.050 | 0.028 |
| 4 | 0.024 | 0.033 | 0.022 | 0.025 | 0.061 | 0.022 |
| 5 | 0.036 | 0.040 | 0.021 | 0.028 | 0.075 | 0.023 |
| 6 | 0.039 | 0.039 | 0.030 | 0.020 | 0.065 | 0.023 |
| 7 | 0.032 | 0.027 | 0.024 | 0.033 | 0.031 | 0.024 |
| 8 | 0.036 | 0.027 | 0.033 | 0.042 | 0.023 | 0.024 |
| 9 | 0.036 | 0.030 | 0.029 | 0.028 | 0.031 | 0.024 |
| 10 | 0.028 | 0.030 | 0.027 | 0.028 | 0.036 | 0.024 |
| mean | 0.031 | 0.031 | 0.027 | 0.031 | 0.049 | 0.025 |

NO: non-obstructed; MO: moderately obstructed; SO: severely obstructed; Varying: as explained in Section 3.2.

mean values and standard deviations of $\epsilon$ over ten cycles is presented in Table 2, which shows little variation.

The results for the adult model with large cannula are depicted in Fig. 10. In both cases, the reconstructed curves are again almost identical to the actual curves. Table 3 shows the values of $\epsilon$ for each of the 10 cycles used to determine the ratio $a_{in}/a_{ex}$ for the large cannula, while the means and standard deviations of $\epsilon$ for the different cannula sizes are shown in Table 4. The cannula size seems to slightly influence the accuracy of the reconstruction. The errors are, in general, decreasing with

**Table 2**
Average and standard deviation (in brackets) of $\epsilon$ for the different cannula sizes and breathing profiles of the infant model.

| Breathing profile | Cannula Size | | |
|---|---|---|---|
| | Small | Medium | Large |
| NO | 0.031 ($5.44{\cdot}10^{-3}$) | 0.030 ($5.29{\cdot}10^{-3}$) | 0.037 ($6.06{\cdot}10^{-3}$) |
| MO | 0.031 ($6.21{\cdot}10^{-3}$) | 0.038 ($6.72{\cdot}10^{-3}$) | 0.043 ($7.09{\cdot}10^{-3}$) |
| SO | 0.027 ($5.19{\cdot}10^{-3}$) | 0.027 ($5.15{\cdot}10^{-3}$) | 0.034 ($7.74{\cdot}10^{-3}$) |
| NO varying | 0.031 ($9.10{\cdot}10^{-3}$) | 0.034 ($5.26{\cdot}10^{-3}$) | 0.039 ($3.86{\cdot}10^{-3}$) |
| MO varying | 0.049 ($1.76{\cdot}10^{-2}$) | 0.050 ($1.10{\cdot}10^{-2}$) | 0.048 ($7.73{\cdot}10^{-3}$) |
| SO varying | 0.025 ($4.12{\cdot}10^{-3}$) | 0.048 ($4.56{\cdot}10^{-3}$) | 0.036 ($7.88{\cdot}10^{-3}$) |

NO: non-obstructed; MO: moderately obstructed; SO: severely obstructed; Varying: as explained in Section 3.2.

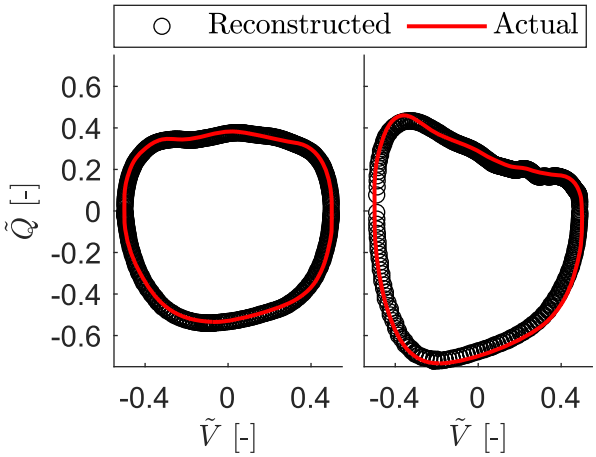


**Fig. 10.** Typical reconstructed and actual scaled flow-volume curves for healthy (left, $\epsilon = 0.027$) and COPD (right, $\epsilon = 0.038$) breathing for the adult model with large cannula.

**Table 3**
Values of $\epsilon$ for adult model with large cannula for ten cycles of the different breathing profiles (see Fig. 5).

| Cycle | Healthy | COPD | Healthy varying | COPD varying |
|---|---|---|---|---|
| 1 | 0.039 | 0.029 | 0.042 | 0.035 |
| 2 | 0.038 | 0.030 | 0.063 | 0.038 |
| 3 | 0.029 | 0.021 | 0.063 | 0.037 |
| 4 | 0.056 | 0.038 | 0.039 | 0.058 |
| 5 | 0.038 | 0.036 | 0.067 | 0.060 |
| 6 | 0.036 | 0.052 | 0.061 | 0.076 |
| 7 | 0.033 | 0.031 | 0.038 | 0.036 |
| 8 | 0.031 | 0.038 | 0.058 | 0.030 |
| 9 | 0.027 | 0.040 | 0.044 | 0.037 |
| 10 | 0.043 | 0.049 | 0.073 | 0.039 |
| mean | 0.037 | 0.036 | 0.055 | 0.044 |

Varying: as explained in Section 3.2.

**Table 4**
Average and standard deviation (in brackets) of $\epsilon$ for the different cannula sizes and breathing profiles of the adult model.

| Breathing profile | Cannula Size | | |
|---|---|---|---|
| | Small | Medium | Large |
| Healthy | 0.080 ($2.06{\cdot}10^{-2}$) | 0.061 ($1.40{\cdot}10^{-2}$) | 0.037 ($8.32{\cdot}10^{-3}$) |
| COPD | 0.046 ($1.47{\cdot}10^{-2}$) | 0.044 ($1.26{\cdot}10^{-2}$) | 0.036 ($9.29{\cdot}10^{-3}$) |
| Healthy varying | 0.063 ($3.49{\cdot}10^{-2}$) | 0.063 ($3.90{\cdot}10^{-2}$) | 0.055 ($1.29{\cdot}10^{-2}$) |
| COPD varying | 0.056 ($1.28{\cdot}10^{-2}$) | 0.055 ($1.34{\cdot}10^{-2}$) | 0.044 ($1.47{\cdot}10^{-2}$) |

Varying: as explained in Section 3.2.

increasing cannula size, and the standard deviation is up to 2.6 times higher when comparing the large to the small cannula.

The influence of the cannula size can be explained by the range of pressures measured: for the adult (with large cannula) these are between -15 and 8 Pa (healthy breathing) or -23 and 10 Pa (COPD), whereas for the infant model (with the small cannula, non-obstructed breathing) pressures are approximately between -120 and 80 Pa. The pressure sensor had a ±0.08% full scale error, which is 5.6 Pa. Compared to the total variation in pressure, this error is about ten times larger for the adult than for the infant model. Fortunately, since this error is random, the general shape of the low-pass filtered pressure, and consequently the scaled flow-volume curves, is not significantly affected by this error. However, minor pressure changes do have a relatively large effect on the values of $\widetilde{Q}$ and $\widetilde{V}$, such that the reconstruction is less accurate. This effect is even stronger for smaller cannulae, where the measured pressures are smaller. Nonetheless, in all cases the difference in shape between healthy and COPD breathing is clear. By using a smaller range pressure sensor with similar full scale error, results could be improved.

Fig. 11 shows the reconstructed (using $T = 60$ seconds) and actual scaled flow rate in time for the random test profile. It is observed that the reconstructed signal is slightly lagging behind the actual signal, which is a result from slight compressibility effects within the cylinder of the breathing simulator and within the upper airway. Apart from that, the reconstructed signal matches the actual signal almost perfectly during expiration. During inhalation, the reconstruction is in general good, but large inspiratory peaks tend to be overestimated. Nonetheless, the test profile shows that the assumed flow behaviour is indeed valid in a more challenging situation with a broad range of flow rates. Although the random profile was not meant as representative breathing, it is possible to determine flow-volume curves from the signal. As before, breathing cycles were determined based on local minima. Additional constraints were added to ensure that the local minima represented a peak in inspiratory flow rate (i.e. minimum was below zero pressure or flow), and that the breathing cycle contained expiration (i.e. positive pressures or flows were present between the starting and ending local minima). It appeared that there were 48 breathing cycles within the 60 s signal. The reconstructed and actual flow-volume curves of these cycles are presented as supplementary material. The average norm over all cycles is 0.077. Although this is higher than the norms observed in the other breathing profiles, a visual comparison shows that the reconstructed curves match the actual curves very well.

## 5. Discussion

In this paper it was shown how scaled respiratory flow rate and volume could be obtained from the pressure difference between a cannula and the atmosphere. By looking at *scaled* flow and volume, the method is self-calibrating for the case-dependent resistance based on the pressure measurements. Experiments on anatomically correct 3D-printed geometries of an infant and an adult demonstrated that the measured pressure difference can indeed be used to accurately reconstruct scaled flow-volume curves.

The basic idea of monitoring respiration by connecting a pressure sensor to a nasal cannula is not new. Compared to the method of Kohler et al. [29,30], where nasal airflow is quantified using a modified nasal cannula, two pressure transducers and a calibration using a nasal mask with attached flow meter, the method presented here offers great advantages in the ease of use: no modifications to the cannula are made, less equipment is used, and there is no need for calibration. Although no quantification of flow and volume can be made, the shape of tidal flow-volume curves is accurately recovered, which is of primary interest from a clinical point of view.

In ref. [9], it was found that the absolute values of commonly used tidal breathing parameters, like peak tidal expiratory flow (PTEF) or tidal volume ($V_T$) were poor predictors in the identification of chronic lung diseases among infants, whereas the shape of the flow-volume curves was found to be significantly different from healthy profiles. Leonhardt et al. [8] presented a set of mathematical features to identify pulmonary diseases from the shape of tidal flow-volume curves. Also scaled tidal breathing parameters, usually based on PTEF and $V_T$, were found useful in the identification of expiratory airway obstruction in infants [7,32]. These scaled parameters can also be obtained from the non-dimensional curves obtained with the newly presented method. A recent study showed that a concave shape of the tidal flow-volume loop in wheezing infants indicated an increased chance of experiencing exacerbations in the following year [31]. Also for adults, concave tidal expiratory profiles were observed in severely obstructed COPD-patients [6].

The method is restricted to nasal breathing, since the pressure difference due to breathing flow rate is only detected in the nose. Moreover, the mouth should be closed during the tests to obtain reliable results. Although it may technically be possible to obtain flow-volume curves during oronasal breathing, it cannot be guaranteed that an increase in breathing flow rate leads to an increase in the pressure difference, as the ratio of nasal to oral flow may change. Therefore, reconstructions obtained with open mouth may be inaccurate, even if there was a flow through the nose. Due to this restriction, some patients may need to be instructed to close their mouth during the test. In infants, where instructions could be problematic, this problem is fortunately circumvented as infants are preferential, if not obligatory, nasal breathers [38]. Also most adults are nasal breathers at rest, although about 13% use oronasal breathing [39]. Even measurements during sleep may be possible, since adults mostly use nasal breathing during sleep [40,41]. However, since oral breathing is added intermittently [41], some periods in the pressure recordings need to be excluded.

This study has two limitations. First, rigid upper airway geometries were used in the experiments, disregarding any elastic effects of the

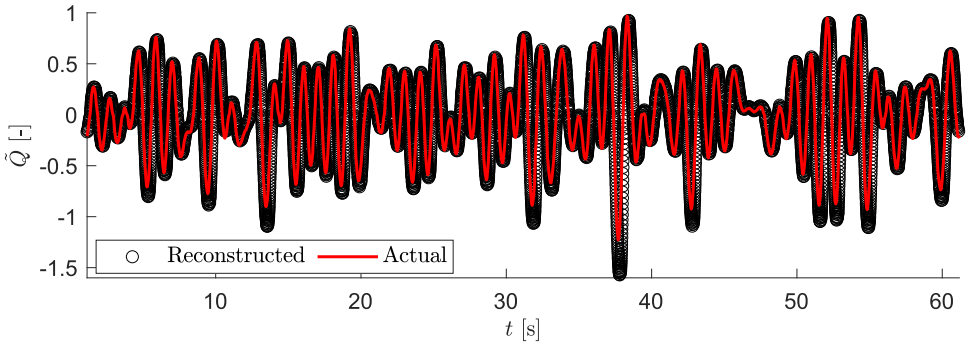


**Fig. 11.** Comparison of the reconstructed and actual scaled flow rate of the random test profile for the infant model with small cannula to demonstrate the robustness of the method. A small time lag is observed due to mild compressibility. Large inspiratory peaks are slightly overestimated, but reconstruction is almost perfect during exhalation.

nostrils. The influence of these effects can be analysed for two different situations. On the one hand, when due to elasticity the nostril walls are at a different but constant position during inspiration and expiration, the effect on the relation between flow-rate and pressure-difference is captured by modifying the values of the conductances $a_{in}$ and $a_{ex}$. However, Eqs. (11) and (13) show that the conductances do not appear in the expressions for $\widetilde{V}$ and $\widetilde{Q}$, and therefore the scaled flow-volume curve will not be affected. On the other hand, when due to elasticity the nostril walls are at a pressure-dependent position during respiration, the effect on the relation between flow-rate and pressure-difference is *not* captured modifying the values of the conductances. In this case one may assume that the nostril wall position depends linearly on pressure:

$$a_{in/ex} = a^{o}_{in/ex} + \Delta a_{in/ex}, \quad \Delta a_{in/ex} \equiv a^{'}_{in/ex}\Delta p, \tag{18}$$

which leads to the following relative error in the computed flow rate:

$$\frac{\Delta Q}{Q_o} = \frac{\Delta a_{in/ex}}{a^{o}_{in/ex}}. \tag{19}$$

Since the nasal valve is the narrowest part of the nose, it is expected to be most significant for the values of $a$. The nasal resistance is inversely proportional to the squared area [42]. On average, the adult nasal valve has an area of 61 $mm^2$ and a compliance of 0.031 $mm^2$/Pa [43]. With the encountered pressure differences in the adult model, it can therefore be concluded that the relative variation in the conductances $a$ will be very small, typically a few percent, and therefore the relative error in the computed flow rate will be a few percent.

The second limitation is the relatively large range of the pressure sensors ($\pm$ 7000 Pa) compared to the encountered pressure differences, especially for the adult model where the cannulas occlude less than 25% of the nostril area. Although the error is random and accurate reconstructions could therefore be obtained from the filtered signal, it is likely that the accuracy of the method for small cannulas can be improved by using a pressure sensor capable of measuring relatively small pressure differences. A range of $\pm$250 to $\pm$500 Pa is considered to be more suitable.

The main purpose of the experiments in this study was to determine the capability of the proposed method to accurately reconstruct flow-volume curves. Therefore, instead of testing on humans, a fully controllable in-vitro setup was used. This allowed for a direct and accurate comparison between actual and reconstructed curves. The results show that the method indeed produces accurate flow-volume curves using $b_{in} = 0.75$ and $b_{ex} = 0.55$ for both the infant and the adult model, and that the error is relatively insensitive to these values. The used respiratory profiles were obtained from tidal breathing humans during earlier studies. The fact that clear differences are observed between the healthy and unhealthy spirometric curves indicates that it is clinically indeed useful to look at tidal spirometric curves. Further research in a clinical setting is required to show the clinical use and applicability of this method.

The method has a great potential use in the long-term monitoring and the identification of obstructive lung diseases, especially for people unable to perform spirometry tests. A restriction of the method is that it requires breathing through the nose. Important advantages of this method over conventional spirometry are the ease of use, the absence of required effort, and good patient comfort. These advantages increase the reproducibility of the measurements.

## 6. Conclusion

This study presents a novel method that, by simply measuring the pressure in the nostrils with a nasal cannula, reconstructs scaled tidal breathing flow-volume curves very accurately. The shapes of these curves can be used to identify and monitor obstructive lung diseases. Tidal breathing avoids the forced expiration manoeuvre required in conventional spirometry, which is associated with limited reliability and repeatability. Compared to other methods that obtain tidal flow-volume curves, this method offers advantages in the ease of use and the automatic continuous calibration, allowing for frequent or even continuous measurements. This method opens the route towards the remote monitoring of patients with chronic lung diseases. In-vivo experiments are required to further assess the clinical applicability of the method.

## Funding

The experimental validation reported in this paper was supported by Longfonds, Fisher & Paykel Healthcare Ltd. and Vivisol Nederland BV, under Longfonds project number 10.1.17.184. The sponsors were not involved in the study design, the collection, analysis and interpretation of data, or the writing or submission of the article.

## Ethical Approval

Not required.

## CRediT authorship contribution statement

**Rutger H.J. Hebbink:** Conceptualization, Methodology, Software, Validation, Investigation, Data curation, Writing – original draft, Writing – review & editing, Visualization. **Rob Hagmeijer:** Conceptualization, Methodology, Investigation, Writing – original draft, Writing – review & editing, Supervision, Project administration, Funding acquisition.

## Declaration of Competing Interest

Hebbink and Hagmeijer report a patent N2026553 pending to University of Twente.

## Acknowledgments

The authors want to express their gratitude to technician S. Wanrooij of the University of Twente for his large contribution in the design and realisation of the experimental set-up. The authors also want to acknowledge P. Van Der Meulen of VDM Kunststoftechniek for his advice and efforts in the 3D-printing of the geometries.

## Supplementary material

Supplementary material associated with this article can be found, in the online version, at 10.1016/j.medengphy.2021.09.004

## References

[1] Richards JA. Office spirometry—indications and limitations. South African Family Practice 2006;48(2):48–51. https://doi.org/10.1080/20786204.2006.10873340.
[2] Global Initiative for Chronic Obstructive Lung Disease I. Global strategy for the diagnosis, management, and prevention of chronic obstructive pulmonary disease (2021 report). Tech. Rep. Global Initiative for Chronic Obstructive Lung Disease, Inc.; 2020.
[3] Miller MR, Hankinson J, Brusasco V, Burgos F, Casaburi R, Coates A, Crapo R, Enright P, van der Grinten CPM, Gustafsson P, Jensen R, Johnson DC, MacIntyre N, McKay R, Navajas D, Pedersen OF, Pellegrino R, Viegi G, Wanger J. Standardisation of spirometry. European Respiratory Journal 2005;26(2):319–38. https://doi.org/10.1183/09031936.05.00034805.
[4] Miller MR. How to interpret spirometry. Breathe 2008;4(3):259–61.
[5] Lødrup Carlsen KC. Tidal breathing at all ages. Monaldi Archives for Chest Disease 2000;55(5):427–34.
[6] Nozoe M, Mase K, Murakami S, Okada M, Ogino T, Matsushita K, et al. Relationship between spontaneous expiratory flow-volume curve pattern and air-flow obstruction in elderly COPD patients. Respir Care 2013;58(10):1643–8. https://doi.org/10.4187/respcare.02296.
[7] Hevroni A, Goldman A, Blank-Brachfeld M, Ahmad WA, Ben-Dov L, Springer C. Use of tidal breathing curves for evaluating expiratory airway obstruction in infants. Journal of Asthma 2018;55(12):1331–7. https://doi.org/10.1080/02770903.2017.1414234.

[8] Leonhardt S, Ahrens P, Kecman V. Analysis of tidal breathing flow volume loops for automated lung-function diagnosis in infants. IEEE Trans Biomed Eng 2010;57(8):1945–53. https://doi.org/10.1109/TBME.2010.2046168.
[9] Schmalisch G, Wilitzki S, Wauer RR. Differences in tidal breathing between infants with chronic lung diseases and healthy controls. BMC Pediatr 2005;5(1):36. https://doi.org/10.1186/1471-2431-5-36.
[10] Morris MJ, Lane DJ. Tidal expiratory flow patterns in airflow obstruction. Thorax 1981;36(2):135–42. https://doi.org/10.1136/thx.36.2.135.
[11] Colasanti RL, Morris MJ, Madgwick RG, Sutton L, Williams EM. Analysis of tidal breathing profiles in cystic fibrosis and COPD. Chest 2004;125(3):901–8. https://doi.org/10.1378/chest.125.3.901.
[12] Morris MJ, Williams EM, Madgwick R, Banerjee R, Phillips E. Changes in lung function and tidal airflow patterns after increasing extrathoracic airway resistance. Respirology 2004;9(4):474–80. https://doi.org/10.1111/j.1440-1843.2004.00612.x.
[13] Wilkens H, Weingard B, Mauro AL, Schena E, Pedotti A, Sybrecht GW, Aliverti A. Breathing pattern and chest wall volumes during exercise in patients with cystic fibrosis, pulmonary fibrosis and COPD before and after lung transplantation. Thorax 2010;65(9):808–14. https://doi.org/10.1136/thx.2009.131409.
[14] Motamedi-Fakhr S, Wilson RC, Iles R. Tidal breathing patterns derived from structured light plethysmography in COPD patients compared with healthy subjects. Medical Devices (Auckland, NZ) 2016;10:1–9. https://doi.org/10.2147/MDER.S119868.
[15] Niérat M-C, Dubé B-P, Llontop C, Bellocq A, Layachi Ben Mohamed L, Rivals I, et al. Measuring ventilatory activity with structured light plethysmography (SLP) reduces instrumental observer effect and preserves tidal breathing variability in healthy and COPD. Front Physiol 2017;8. https://doi.org/10.3389/fphys.2017.00316.
[16] Laveneziana P, Llontop C, Nierat M-C, Bellocq A, Straus C, Similowski T. Disruption of tidal breathing in COPD by use of pneumotachograph and mouthpiece compared to non-contact measurement with structured light plethysmography (SLP). European Respiratory Journal 2015;46(suppl 59):PA511. https://doi.org/10.1183/13993003.congress-2015.PA511.
[17] Brown K, Aun C, Jackson E, Mackersie A, Hatch D, Stocks J. Validation of respiratory inductive plethysmography using the qualitative diagnostic calibration method in anaesthetized infants. European Respiratory Journal 1998;12(4):935–43.
[18] Parreira VF, Vieira DSR, Myrrha MAC, Pessoa IMBS, Lage SM, Britto RR. Optoelectronic plethysmography: a review of the literature. Rev Bras Fisioter Nov-Dec 2012;16(6):439–53.
[19] Reinaux CMA, Aliverti A, da Silva LGM, da Silva RJ, Gonçalves JN, Noronha JB, et al. Tidal volume measurements in infants: opto-electronic plethysmography versus pneumotachograph. Pediatr Pulmonol 2016;51(8):850–7. https://doi.org/10.1002/ppul.23394.
[20] Lauhkonen E, Cooper BG, Iles R. Mini review shows that structured light plethysmography provides a non-contact method for evaluating breathing patterns in children. Acta Paediatr 2019;108(8):1398–405. https://doi.org/10.1111/apa.14769.
[21] Porojan-Suppini N, Fira-Mladinescu O, Marc M, Tudorache E, Oancea C. Lung function assessment by impulse oscillometry in adults. Ther Clin Risk Manag 2020;16:1139–50. https://doi.org/10.2147/TCRM.S275920.
[22] Brashier B, Salvi S. Measuring lung function using sound waves: role of the forced oscillation technique and impulse oscillometry system. Breathe 2015;11(1):57–65. https://doi.org/10.1183/20734735.020514.
[23] Goldman MD. Clinical application of forced oscillation. Pulmonary Pharmacology & Therapeutics 2001;14(5):341–50. https://doi.org/10.1006/pupt.2001.0310.
[24] Norman RG, Ahmed MM, Walsleben JA, Rapoport DM. Detection of respiratory events during NPSG: nasal cannula/pressure sensor versus thermistor. Sleep 1997;20(12):1175–84. https://doi.org/10.1093/sleep/20.12.1175.
[25] Ayappa I, Norman RG, Krieger AC, Rosen A, O'Malley RL, Rapoport DM. Non-invasive detection of respiratory effort-related arousals (RERAs) by a nasal cannula/pressure transducer system. Sleep 2000;23(6):763–71. https://doi.org/10.1093/sleep/23.6.763.
[26] Thurnheer R, Xie X, Bloch KE. Accuracy of nasal cannula pressure recordings for assessment of ventilation during sleep. Am J Respir Crit Care Med 2001;164(10):1914–9. https://doi.org/10.1164/ajrccm.164.10.2102104.
[27] Serebrisky D, Cordero R, Mandeli J, Kattan M, Lamm C. Assessment of inspiratory flow limitation in children with sleep-disordered breathing by a nasal cannula pressure transducer system. Pediatr Pulmonol 2002;33(5):380–7. https://doi.org/10.1002/ppul.10096.
[28] Hosselet J-J, Norman RG, Ayappa I, Rapoport DM. Detection of flow limitation with a nasal cannula/ pressure transducer system. Am J Respir Crit Care Med 1998;157(5):1461–7. https://doi.org/10.1164/ajrccm.157.5.9708008.
[29] Kohler M, Thurnheer R, Bloch KE. Non-invasive, side-selective nasal airflow monitoring. Physiol Meas 2005;26(1):69–82. https://doi.org/10.1088/0967-3334/26/1/007.
[30] Kohler M, Thurnheer R, Bloch KE. Side-selective, unobtrusive monitoring of nasal airflow and conductance. J Appl Physiol 2006;101(6):1760–5. https://doi.org/10.1152/japplphysiol.00517.2006.
[31] Keklikian E, Cornes P, Cela CJ, Sanchez Solis M, García Marcos L, Castro-Rodriguez JA. Predicting the outcome of respiratory disease in wheezing infants using tidal flow-volume loop shape. Allergol Immunopathol (Madr) 2020;48(4):355–9. https://doi.org/10.1016/j.aller.2019.12.002.
[32] Banovcin P, Seidenberg J, Der Hardt HV. Assessment of tidal breathing patterns for monitoring of bronchial obstruction in infants. Pediatr Res 1995;38(2):218–20. https://doi.org/10.1203/00006450-199508000-00014.
[33] Janssens HM, de Jongste JC, Fokkens WJ, Robben SGF, Wouters K, Tiddens HAWM. The sophia anatomical infant nose-throat (saint) model: a valuable tool to study aerosol deposition in infants. Journal of Aerosol Medicine 2001;14(4):433–41. https://doi.org/10.1089/08942680152744640.
[34] embodi3D.com. Easily Create 3D Printable Muscle and Skin STL Files from Medical CT Scans. https://www.embodi3d.com/blogs/entry/353-easily-create-3d-printable-muscle-and-skin-stl-files-from-medical-ct-scans/; 2016.
[35] Van Hove SC, Storey J, Adams C, Dey K, Geoghegan PH, Kabaliuk N, et al. An experimental and numerical investigation of CO2 distribution in the upper airways during nasal high flow therapy. Ann Biomed Eng 2016;44(10):3007–19. https://doi.org/10.1007/s10439-016-1604-8.
[36] Womersley JR. Method for the calculation of velocity, rate of flow and viscous drag in arteries when the pressure gradient is known. J Physiol (Lond) 1955;127(3):553–63. https://doi.org/10.1113/jphysiol.1955.sp005276.
[37] Uchida S. The pulsating viscous flow superposed on the steady laminar motion of incompressible fluid in a circular pipe. Zeitschrift für angewandte Mathematik und Physik ZAMP 1956;7(5):403–22. https://doi.org/10.1007/BF01606327.
[38] Bergeson PS, Shaw JC. Are infants really obligatory nasal breathers? Clin Pediatr (Phila) 2001;40(10):567–9. https://doi.org/10.1177/000992280104001006.
[39] Niinimaa V, Cole P, Mintz S, Shephard RJ. The switching point from nasal to oronasal breathing. Respir Physiol 1980;42(1):61–71. https://doi.org/10.1016/0034-5687(80)90104-8.
[40] Fitzpatrick MF, Driver HS, Chatha N, Voduc N, Girard AM. Partitioning of inhaled ventilation between the nasal and oral routes during sleep in normal subjects. J Appl Physiol 2003;94(3):883–90. https://doi.org/10.1152/japplphysiol.00658.2002.
[41] Madronio MR, Somma ED, Stavrinou R, Kirkness JP, Goldfinch E, Wheatley JR, Amis TC. Older individuals have increased oro-nasal breathing during sleep. European Respiratory Journal 2004;24(1):71–7. https://doi.org/10.1183/09031936.04.00004303.
[42] Warren DW, Hairfield WM, Seaton DL, Hinton VA. The relationship between nasal airway cross-sectional area and nasal resistance. American Journal of Orthodontics and Dentofacial Orthopedics 1987;92(5):390–5. https://doi.org/10.1016/0889-5406(87)90259-9.
[43] O'Neill G, Tolley NS. The complexities of nasal airflow: theory and practice. J Appl Physiol 2019;127(5):1215–23. https://doi.org/10.1152/japplphysiol.01118.2018.